

# Enabling Full-Duplex LEO Satellite Systems with Non-Reciprocal BD-RIS-Assisted Beamforming

Ziang Liu, Wonjae Shin, *Senior Member, IEEE* and Bruno Clerckx, *Fellow, IEEE*

**Abstract**—Low Earth orbit (LEO) satellite is a promising technology for providing low-latency, high-data-rate, and wide-coverage communication services. However, the high mobility of LEO satellites necessitates fast and accurate beam steering to continuously serve ground devices. While large antenna arrays can address these challenges, strict constraints on power, size, and weight make such solutions difficult to implement. Furthermore, future non-terrestrial networks (NTNs) require high spectral efficiency, which motivates the adoption of in-band full-duplex (FD) systems. To overcome these challenges, we propose an FD LEO satellite system, where the non-reciprocal beyond-diagonal reconfigurable intelligent surfaces (NR-BD-RIS) and multiple transmit and receive antennas are attached to the LEO satellite. The NR-BD-RIS reflects the downlink (DL) and uplink (UL) signals by passive beamforming. By incorporating non-reciprocal components into the impedance network of RIS, the NR-BD-RIS breaks channel reciprocity, facilitating simultaneous support for multiple beam directions. To cover a wide coverage, we propose a time-sharing scheduling framework where, in each time slot, the NR-BD-RIS simultaneously serves multiple DL and multiple UL ground devices. An optimization problem is defined to maximize the weighted sum-rate over the entire scheduling period. Numerical results demonstrate that the proposed NR-BD-RIS significantly performs better than both conventional BD-RIS and diagonal RIS (D-RIS) regarding DL and UL sum-rate performance under both single-user (SU) and multiple-user (MU) cases. Additionally, the NR-BD-RIS requires less frequent reconfiguration compared to other two types of RIS, making it more practical for implementation.

**Index Terms**—Full-duplex (FD), low Earth orbit (LEO) satellite, non-reciprocal beyond-diagonal reconfigurable intelligent surface (NR-BD-RIS)

## I. INTRODUCTION

Low Earth orbit (LEO) satellite system, operating at altitudes of 500–2000 km, offer low latency, high data rates, and wide coverage, making it a promising solution for ubiquitous, high-capacity global connectivity in current and future wireless networks [1]. However, the high mobility results in short visibility times, necessitating dynamic and precise control of beam directions to continuously serve ground devices [2]. Achieving this requires large antenna arrays with high directional gain, but the power, size, and weight constraints of LEO satellites make deploying such arrays challenging [1]. Furthermore, future non-terrestrial networks (NTNs) demand efficient spectrum use, motivating in-band full-duplex (FD) operation [3], which can potentially double spectral efficiency

Z. Liu, and B. Clerckx are with the Communications & Signal Processing (CSP) Group at the Department of Electrical and Electronic Engineering, Imperial College London, SW7 2AZ, UK. (e-mails: {ziang.liu20, b.clerckx}@imperial.ac.uk). W. Shin is with the School of Electrical Engineering, Korea University, Seoul 02841, South Korea (e-mail: wjshin@korea.ac.kr). (Corresponding author: W. Shin)

by enabling simultaneous transmission and reception. These factors motivate the need for FD LEO satellite systems with energy efficiency, low cost, and high spectrum usage.

Reconfigurable intelligent surfaces (RIS) have obtained extensive attention in both academia and industry due to their capability to intelligently manipulate the wireless propagation environment, therefore enabling high energy and spectrum efficiency [4]. Furthermore, RIS is a low-cost planar surface consisting of passive, reconfigurable scattering elements, making its integration into LEO satellites a promising approach to satisfy the strict requirements of FD LEO satellite systems [1]. Several studies have examined the utilization of RIS for improving LEO satellite communication performance. For instance, [1] proposes a RIS-assisted LEO satellite system to achieve energy-efficient transmission. Additionally, a delay-adjustable RIS (DA-RIS) is introduced in [5] to realize a frequency prism, addressing size, weight, and power (SWaP) constraints while improving beam flexibility.

From a technical perspective, we can use an array of scattering elements connected to reconfigurable impedance network to model RIS. In the diagonal RIS (D-RIS), each port of the impedance network is connected to ground through a single impedance component. This architecture, also referred to as single-connected RIS [6], leads to a diagonal scattering matrix. Consequently, the D-RIS can only adjust the phase of the incident wave at each port, limiting its passive beamforming capabilities. To address the limitations of controlling only the phase of the incident wave, [6]–[8] introduce beyond-diagonal (BD)-RIS. Different from D-RIS, the impedance network ports of BD-RIS are interconnected, allowing the output wave at one port to depend not only on the wave impinging on that port but also on waves from neighboring ports. These interconnections lead to a non-diagonal scattering matrix. BD-RIS has demonstrated significant improvements in spectrum and energy efficiency for wireless communications [6], [7], and improved performance in sensing and localization systems [9]. However, the interconnection of all ports and the required impedance components increase circuit complexity. To achieve a trade-off between hardware complexity and system performance, prior work [6] has introduced the group-connected (GC)-BD-RIS, where ports are interconnected within groups, leading to a block-diagonal scattering matrix. Further advancements include tree-connected and forest-connected BD-RIS structures proposed in [10], which demonstrate a better trade-off between circuit complexity and performance in single-user multiple-input single-output (MISO) systems. Additionally, optimal architectures that are band-connected and stem-connected BD-RISs, which show improved trade-offs in multi-user multiple-

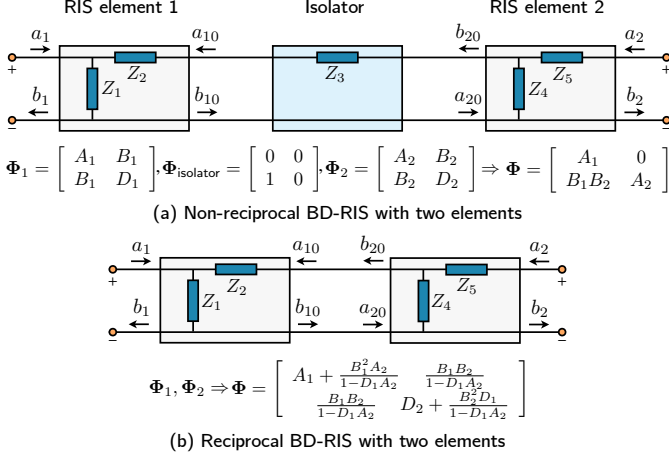


Fig. 1. Illustration of 2-port (a) NR-BD-RIS, and (b) R-BD-RIS, where  $\Phi_1$ ,  $\Phi_2$  and  $\Phi_{\text{isolator}}$  are the scattering matrices of the RIS element 1, 2 and isolator, respectively. Based on  $\Phi_1$ ,  $\Phi_2$  and  $\Phi_{\text{isolator}}$ , we can obtain the overall scattering matrix  $\Phi$  of the  $2 \times 2$  BD-RIS.

input multiple-output (MIMO) systems, have been introduced in [11], [12].

Circuit reciprocity in the impedance network is a commonly assumed feature in widely-used RIS models, as the impedance between two ports is identical in both directions. This results in a symmetric scattering matrix and channel reciprocity, meaning the signal path from the transmit (Tx) to the receive (Rx) is identical to that from the Rx to the Tx. While reciprocal RISs, including D-RIS and reciprocal (R)-BD-RIS, have been extensively studied in the literature [6], [7], [9], [10], channel reciprocity imposes limitations on simultaneously serving non-aligned downlink (DL) and uplink (UL) devices [13], which is a common scenario in FD LEO satellite systems. To resolve this constraint, breaking circuit reciprocity is a natural solution, as it disrupts channel reciprocity. Consequently, the reversibility of signal paths is disrupted, enabling support for different signal propagation directions. This capability is particularly beneficial in FD LEO satellite systems, where DL and UL devices are often non-aligned.

Several efforts have been made to realize non-reciprocal (NR)-BD-RIS, such as adding non-reciprocal components [14], [15], e.g., isolators or circulators, into the impedance network of RIS. In Fig. 1, we demonstrate the 2-port impedance networks and their corresponding scattering matrices of both NR-BD-RIS achieved by isolator and R-BD-RIS [14], [15]. In addition, utilizing radio frequency (RF) micro-electromechanical systems (MEMs) switches [16], [17], and employing metasurface-based techniques [18]–[21] can also break the circuit reciprocity. These hardware advancements have enabled NR-BD-RIS to improve channel gain [16], achieve spatial selectivity [22], and facilitate secure communications [23], [24]. A key area of research focuses on supporting non-aligned DL and UL devices in FD systems. For example, [13] theoretically demonstrates that NR-BD-RIS enables optimally simultaneous maximization of DL and UL channel gains in single-antenna FD systems, a capability that R-BD-RIS and D-RIS are unable to achieve. Further studies

such as [25] show that NR-BD-RIS achieves better DL and UL sum-rate performance than other two types of RIS in multi-user multiple-antenna FD systems. Additionally, [26] proposes a secure FD wireless circulator, which allows one-way secure communication. Building on these work, as depicted in Fig. 2, we propose an NR-BD-RIS-enabled FD LEO satellite system with non-aligned Tx and Rx antennas, addressing the needs for energy efficiency, low cost, and high spectral efficiency in FD LEO satellite systems.

**Contributions and Overview of Results.** The contributions of this paper are listed below:

- To achieve high energy and spectral efficiency with low-cost hardware in FD communications, which are challenging to realize using large antenna arrays or conventional RIS, we propose employing NR-BD-RIS in FD LEO satellite systems. Given the severe path loss in satellite communications, the received uplink power is typically low. Thus, the ratio between self-interference (SI) and uplink signal power is high, making SI mitigation crucial. Therefore, we consider non-aligned Tx and Rx antennas, as illustrated in Fig. 2 (b), to realize propagation-domain SI cancellation. Due to the proximity between the Tx/Rx antennas and the NR-BD-RIS, a near-field channel model is adopted. We incorporate a RIS-assisted satellite far-field channel model. To ensure broad coverage, we design a time-sharing scheduling framework where, in each slot, the NR-BD-RIS serves multiple DL and UL devices in part of the coverage area, and over the full period, it covers the entire area. The antenna setups, channel models, and time-sharing scheduling framework make our work different from [13], [25], [26].
- To address the wide coverage requirements of LEO satellites, we propose a time-sharing scheduling framework that ensures complete area coverage over multiple time slots. Specifically, we formulate a weighted DL and UL sum-rate maximization problem over the entire scheduling period. The optimization variables include the scattering matrix and the Tx and Rx beamforming matrices. To solve this problem, we design an iterative method that updates these variables using a block coordinate descent (BCD) combined with the penalty dual decomposition (PDD) method. Unlike prior works on NR-BD-RIS in [25], [26], the proposed algorithm is designed to the time-sharing scheduling framework.
- Numerical results demonstrate that NR-BD-RIS outperforms both R-BD-RIS and D-RIS regarding DL and UL sum-rate performance in single-user (SU) and multi-user (MU) FD LEO satellite systems, even when the Tx and Rx antennas are not perfectly aligned. Furthermore, by analyzing the average DL and UL sum-rate, we show that NR-BD-RIS requires less frequent reconfiguration compared to other two types of RIS, reducing the burden of real-time impedance reconfiguration and enhancing the practicality of the proposed approach. Additionally, the DL and UL weighted sum-rate performance of NR-BD-RIS improves as the number of RIS elements and the group size of BD-RIS increase. We attribute the advantages of NR-BD-RIS to the additional degrees of freedom due to non-reciprocity,

enabling simultaneous support for multiple beam directions and non-aligned DL and UL devices. Moreover, the robustness of NR-BD-RIS to SI is analyzed, and the results show that it performs better than R-BD-RIS and D-RIS when the SI power level is below 45 dB.

**Organization.** The organization of this paper is given below. We present the system and channel models in Section II. In III, we formulate the optimization problem and develop the proposed solution. Numerical evaluations are provided in IV. Lastly, we conclude this work in V.

**Notation.** We use  $\mathbb{R}$  and  $\mathbb{C}$  to denote the sets of real and complex numbers. Matrices are written in bold uppercase letters, vectors in bold lowercase letters, and scalar quantities in regular font. The operator  $\Re\{\cdot\}$  extracts the real part of a complex quantity. For any matrix  $\mathbf{X}$ , the symbols  $\mathbf{X}^*$ ,  $\mathbf{X}^\top$ ,  $\mathbf{X}^H$ , and  $\mathbf{X}^{-1}$  denote its conjugate, transpose, Hermitian transpose, and inverse. The entry of  $\mathbf{X}$  at position  $(i, j)$  is written as  $[\mathbf{X}]_{i,j}$ . The identity matrix and the all-zero matrix are denoted by  $\mathbf{I}$  and  $\mathbf{0}$ . The operators  $\text{vec}(\cdot)$ ,  $\text{diag}(\cdot)$ ,  $\text{blkdiag}(\cdot)$ ,  $\text{Tr}(\cdot)$ , and  $\otimes$  correspond to vectorization, diagonal construction, block-diagonal construction, trace, and the Kronecker product.

## II. SYSTEM MODEL

As shown in Fig. 2 (a), we consider a FD LEO satellite system enabled by NR-BD-RIS. The LEO satellite is equipped with  $N$  Tx and Rx antennas. The Tx and Rx antenna are set to be non-aligned as shown in Fig. 2(b), which is beneficial to reduce the SI in the propagation domain. The  $K$  DL single-antenna devices are indexed by  $\mathcal{K} \triangleq \{1, \dots, K\}$  and  $I$  UL single-antenna devices are indexed by  $\mathcal{I} \triangleq \{1, \dots, I\}$ . The coverage for all the DL/UL devices is achieved through time-sharing beam control. At the  $\ell^{\text{th}}$  time slot, where  $\ell \in \mathcal{L} \triangleq \{1, \dots, L\}$  denotes the time index, the FD LEO satellite serves one group of DL devices with different transmitted data and one group of UL devices with different uploaded data.

Specifically, the DL and UL devices are both grouped into  $L$  groups. The group of DL devices is indexed by  $p$ , where  $p \in \mathcal{L}$ . The set of the  $p^{\text{th}}$  DL group is denoted by  $\mathcal{G}_{d,p}$ . Similarly, the group of UL devices is indexed by  $q$ , where  $q \in \mathcal{L}$ . The set of the  $q^{\text{th}}$  UL group is represented by  $\mathcal{G}_{u,q}$ . Each DL/UL device only belongs to one group, i.e.,  $\bigcup_{p \in \mathcal{L}} \mathcal{G}_{d,p} = \mathcal{K}$  and  $\mathcal{G}_{d,p} \cap \mathcal{G}_{d,m} = \emptyset$ ,  $\forall p, m \in \mathcal{L}$  and  $p \neq m$  for DL devices.  $\bigcup_{q \in \mathcal{L}} \mathcal{G}_{u,q} = \mathcal{I}$  and  $\mathcal{G}_{u,q} \cap \mathcal{G}_{u,n} = \emptyset$ ,  $\forall q, n \in \mathcal{L}$  and  $q \neq n$  for UL devices. The size of each DL and UL group is defined by  $G_{d,p} = |\mathcal{G}_{d,p}|$  and  $G_{u,q} = |\mathcal{G}_{u,q}|$ , respectively. We also define  $\mu_d : \mathcal{K} \rightarrow \mathcal{L}$  and  $\mu_u : \mathcal{I} \rightarrow \mathcal{L}$  to map the DL and UL devices to its belonging groups, such that  $\mu_d(k) = p, \forall k \in \mathcal{G}_{d,p}$  and  $\mu_u(i) = q, \forall i \in \mathcal{G}_{u,q}$ .

The RIS is modeled as a uniform planar array (UPA) with  $d_v, d_h \in [\frac{\lambda}{10}, \frac{\lambda}{2}]$  spacing along the vertical and horizontal axes, where  $\lambda$  is the carrier wavelength [27]. The RIS consists of  $M = M_v \times M_h$  elements, where  $M_v$  and  $M_h$  are the number of elements in the vertical and horizontal directions, respectively. The length of the RIS is indicated by  $L_v = M_v d_v$ , and the width of the RIS is denoted by  $L_h = M_h d_h$ . The RIS is

placed on the plane of the  $y$  and  $z$  axes, with the reference point set at the center of the RIS. We assume the Tx and Rx antenna arrays are parallel to the  $y$ -axis and are uniform linear arrays (ULAs) consisting of  $N$  elements with  $d_a \in [\frac{\lambda}{10}, \frac{\lambda}{2}]$  spacing. We consider the Tx/Rx antenna to be in the near-field (Fresnel) region of the RIS, and the channel between the Tx antenna and the RIS is modeled as a spherical wavefront [28], [29]. The Rayleigh distance is given by  $r_R = \frac{2(L_v^2 + L_h^2)}{\lambda}$ , and the near-field region refers to the area inside this distance [30]. The BD-RIS has the scattering matrix  $\Phi \in \mathbb{C}^{M \times M}$ . The parameter  $M_g$  denotes the group size, and the scattering matrix is divided into  $G = M/M_g$  groups. The GC-BD-RIS structure can be written in the form  $\Phi = \text{blkdiag}(\Phi_1, \dots, \Phi_G)$ .

### A. Channel Model

1) *Near-field Channel Model:* We consider the channel between the Tx/Rx antenna and the RIS to be in the near-field region due to the short distance. We also assume that the ground devices each have a single antenna. The channel is modeled using a finite-dimensional representation based on the near-field channel model [28], [29]. The parameters of each path in the channel model are set to be fixed during the channel coherence time. As depicted in Fig. 3, the RIS is attached to the plane of the  $y$  and  $z$  axes, with the reference point set at the center of the RIS. The indexing of the RIS elements starts from the bottom-left corner, proceeding in a row by row order. Specifically, the  $m^{\text{th}}$  element is indexed as  $m = (m_h - 1)M_v + m_v$ , where  $m_h \in \mathcal{M}_h \triangleq [1, \dots, M_h]$  and  $m_v \in \mathcal{M}_v \triangleq [1, \dots, M_v]$  denote the horizontal and vertical indices of the element, respectively. Additionally,  $m_h = \left\lfloor \frac{m-1}{M_v} \right\rfloor + 1$ ,  $m_v = \text{mod}(m-1, M_v) + 1$ . The Cartesian coordinates of the  $m^{\text{th}}$  RIS element are given by

$$\mathbf{c}_m = [0, (m_h - \frac{M_h + 1}{2})d_h, (m_v - \frac{M_v + 1}{2})d_v]^\top. \quad (1)$$

We assume the Tx antenna array is a ULA oriented parallel to the  $y$ -axis. The index of the Tx antenna array starts from the left. The reference point of the Tx antenna is located at its center, and the position of the reference point can be described in the polar coordinate system as  $\mathbf{p} = [\theta, \beta, r]^\top$ .  $\theta$  is the azimuth angle,  $\beta$  is the elevation angle, and  $r$  is the distance between the reference point of Tx antenna and the origin of the coordinate system, i.e.,  $\mathbf{c}_0 = [0, 0, 0]^\top$ . The Cartesian coordinates of the  $n^{\text{th}}$  Tx antenna can be expressed as

$$\mathbf{r}_n = [r \sin \beta \sin \theta, r \sin \beta \cos \theta - \frac{(N-1)d_a}{2} + (n-1)d_a, r \cos \beta]^\top. \quad (2)$$

Thus, under the spherical wavefront model, the channel from the  $n^{\text{th}}$  Tx/Rx antenna element to the  $m^{\text{th}}$  RIS element can be written as

$$[\mathbf{G}]_{m,n} = g_{m,n} e^{-j \frac{2\pi}{\lambda} \|\mathbf{r}_n - \mathbf{c}_m\|}, \quad (3)$$

where  $g_{m,n} = \frac{1}{4\pi \|\mathbf{r}_n - \mathbf{c}_m\|}$  is the free-space path-loss coefficient between the  $n^{\text{th}}$  Tx/Rx antenna element and the  $m^{\text{th}}$  RIS element [31], and  $\|\mathbf{r}_n - \mathbf{c}_m\|$  is the Euclidean distance between the Tx antenna and the  $m^{\text{th}}$  element of the RIS.

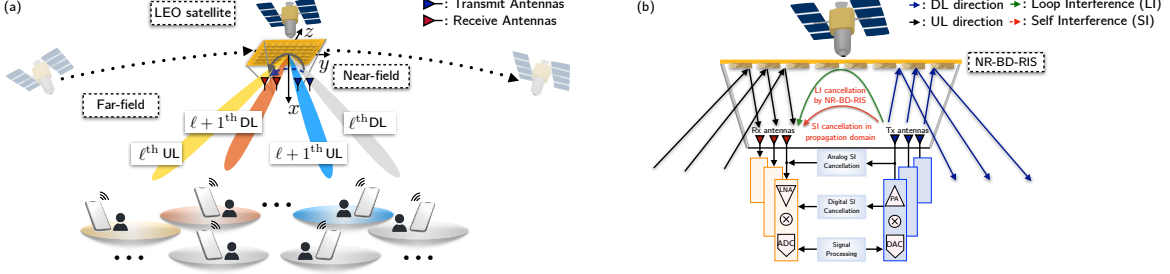


Fig. 2. (a) System model of a FD LEO satellite communication system enabled by the NR-BD-RIS. (b) The non-aligned transmit and receive antennas with the NR-BD-RIS on-board the LEO satellite.

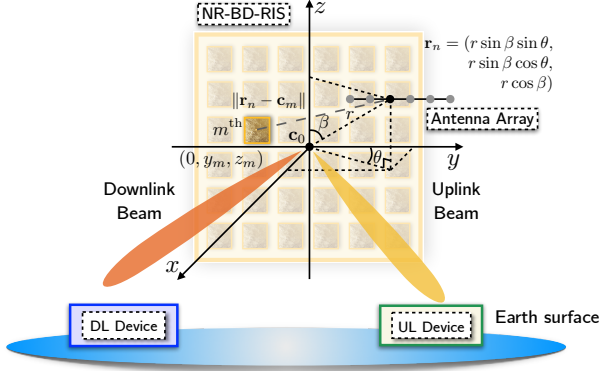


Fig. 3. The coordinate system of the BD-RIS channel model. The NR-BD-RIS can support non-aligned downlink and uplink devices simultaneously.

2) *Satellite Communication Channel Model.* The satellite communication channel model is adopted between the BD-RIS and the device. Satellite communications generally have line-of-sight (LoS) propagation. Therefore, the Rician fading model is utilized in satellite communications [2], given by

$$\mathbf{h} = g_{\text{sat}} \sqrt{\frac{\kappa}{\kappa + 1}} \mathbf{h}_{\text{LoS}} + g_{\text{sat}} \sqrt{\frac{1}{\kappa + 1}} \mathbf{h}_{\text{NLoS}}, \quad (4)$$

where  $\kappa$  is the Rician factor, and  $g_{\text{sat}} = (PL_{\text{BF}} PL_{\text{rain}})^{-1}$  is the path loss coefficient consisting of free space loss, radiation pattern, and rain attenuation.

**Path Loss Model.** Taking the channel from the RIS to the ground device as an example, if the Tx antenna is in the near-field region of the RIS, the path loss model used for the near-field beamforming scheme [2], [27] in an RIS-assisted satellite system is written as:

$$PL_{\text{BF}} = \frac{64\pi^3}{G_t G_r d_v d_h \lambda^\eta A^\eta \left| \sum_{m=1}^M \frac{\sqrt{F_m^{\text{cmb}}}}{r_{tx} r_{rx}} \right|^\eta}, \quad (5)$$

where  $G_t$  and  $G_r$  are the antenna gains of the transmitter and receiver, respectively.  $\eta$  denotes the path loss exponent, and  $A$  is the reflection coefficient amplitude of each RIS element. The distances from the transmitter to the RIS and from the RIS to the receiver are represented by  $r_{tx}$  and  $r_{rx}$ , respectively. Specifically,  $r_{rx}$  is calculated as:

$$r_{rx} = -r_e \sin(\theta_e) + \sqrt{r_e^2 \sin^2(\theta_e) + d_{\text{sat}}^2 + 2r_e d_{\text{sat}}}, \quad (6)$$

where  $r_e$  is the radius of the Earth,  $d_{\text{sat}}$  is the height of the satellite above the Earth, and  $\theta_e$  is the elevation angle (i.e., the angle with respect to (w.r.t) the positive axis) between the RIS and the ground device.  $F_m^{\text{cmb}}$  is the normalized power radiation pattern of the received signal power, which is given by

$$F_m^{\text{cmb}} = F^{\text{tx}}(\vartheta_m^{\text{tx}}, \gamma_m^{\text{tx}}) F(\vartheta_m^{\text{t}}, \gamma_m^{\text{t}}) F(\vartheta_m^{\text{r}}, \gamma_m^{\text{r}}) F^{\text{rx}}(\vartheta_m^{\text{rx}}, \gamma_m^{\text{rx}}), \quad (7)$$

where  $F(\vartheta, \gamma)$  is the normalized radiation pattern for the elevation angle  $\vartheta$  (i.e., the angle w.r.t the positive axis) and the azimuth angle  $\gamma$ .  $F(\vartheta, \gamma)$  is defined as [32]

$$F(\vartheta, \gamma) = \begin{cases} \cos^3 \vartheta & \vartheta \in [0, \frac{\pi}{2}], \gamma \in [0, 2\pi] \\ 0 & \vartheta \in (\frac{\pi}{2}, \pi], \gamma \in [0, 2\pi] \end{cases}. \quad (8)$$

The angles  $\vartheta_m^{\text{tx}}$ ,  $\gamma_m^{\text{tx}}$ , and  $\vartheta_m^{\text{rx}}$ ,  $\gamma_m^{\text{rx}}$  denote the elevation and azimuth angles from the transmitting and receiving antennas to the  $m^{\text{th}}$  RIS element, respectively. Similarly,  $\vartheta_m^{\text{t}}$ ,  $\gamma_m^{\text{t}}$ , and  $\vartheta_m^{\text{r}}$ ,  $\gamma_m^{\text{r}}$  represent the elevation and azimuth angles from the  $m^{\text{th}}$  RIS element to the transmitter and receiver, respectively.

**Rain attenuation.** Rain plays a critical role in influencing satellite communication channels, as it leads to both scattering and absorption of electromagnetic waves as they travel through the atmosphere. The rain attenuation is modeled as [33]

$$PL_{\text{rain}} = \xi_R L_E \text{ (dB)}, \quad (9)$$

where  $\xi_R$  and  $L_E$  denote the specific frequency-dependent coefficient [34] and the effective path length.

## B. Signal Model

During a single time slot  $\ell$ , the FD LEO system simultaneously serves multiple DL and UL devices. For the  $k^{\text{th}}$  DL device, the transmitted signal  $s_k$  is sent at time index  $\ell$ . The effective channel between the Tx antenna and the  $k^{\text{th}}$  DL device is defined as  $\tilde{\mathbf{h}}_{d,k}^{\top} \triangleq \mathbf{h}_{d,k}^{\top} \Phi \mathbf{G}_d \in \mathbb{C}^{1 \times N}$ , where  $\mathbf{h}_{d,k} \in \mathbb{C}^{M \times 1}$  represents the channel from the BD-RIS to the  $k^{\text{th}}$  DL device, and  $\mathbf{G}_d \in \mathbb{C}^{M \times N}$  denotes the channel between the BD-RIS and the Tx antenna. Consequently, the received signal at the  $k^{\text{th}}$  DL device is given by:

$$y_k = \tilde{\mathbf{h}}_{d,k}^{\top} \mathbf{p}_k s_k + \tilde{\mathbf{h}}_{d,k}^{\top} \underbrace{\sum_{j \in \mathcal{G}_{d,p}, j \neq k} \mathbf{p}_j s_j + n_k}_{\text{MU Interference}}, \quad \forall k \in \mathcal{K}, \quad (10)$$

where  $p = \mu_d(k)$  indicates that the  $k^{\text{th}}$  DL device belongs to the  $p^{\text{th}}$  group, and  $n_k \sim \mathcal{CN}(0, \sigma^2)$  represents the additive white Gaussian noise (AWGN) at the  $k^{\text{th}}$  DL device.

In the UL direction, the Rx antenna receives the signal,  $x_j$ , from the  $i^{\text{th}}$  UL device, which is reflected by the BD-RIS. Additionally, the Rx antenna receives SI due to coupling between the Tx and Rx [35], as well as loop interference caused by the BD-RIS reflecting the transmitted signal. We also define the effective channel between  $i^{\text{th}}$  UL user and Rx antenna as  $\tilde{\mathbf{h}}_{u,i} \triangleq \mathbf{G}_u^\top \Phi \mathbf{h}_{u,i} \in \mathbb{C}^{N \times 1}$ , where  $\mathbf{G}_u \in \mathbb{C}^{M \times N}$  is the channel between BD-RIS and Rx antenna. The received signal are subsequently processed using a combiner  $\mathbf{W} \triangleq [\mathbf{w}_1, \dots, \mathbf{w}_I] \in \mathbb{C}^{N \times I}$ . Hence, the received signal at the Rx antenna from the  $i^{\text{th}}$  UL device in  $q^{\text{th}}$  group ( $q = \mu_u(i)$ ) is expressed as:

$$z_i = \sqrt{P_u} \mathbf{w}_i^H \tilde{\mathbf{h}}_{u,i} x_i + \sqrt{P_u} \underbrace{\sum_{v \in \mathcal{G}_{u,q}, v \neq i} \mathbf{w}_i^H \tilde{\mathbf{h}}_{u,v} x_v}_{\text{MU Interference}} + \underbrace{\mathbf{w}_i^H \mathbf{H}_{\text{SI}} \mathbf{p}_s}_{\text{Self-interference}} + \underbrace{\mathbf{w}_i^H \mathbf{G}_u^\top \Phi \mathbf{G}_d \mathbf{p}_s}_{\text{Loop interference}} + \mathbf{w}_i^H \mathbf{n}_u, \quad \forall i \in \mathcal{I}, \quad (11)$$

where  $\mathbf{H}_{\text{SI}} \in \mathbb{C}^{N \times N}$  denotes the SI channel, and  $\mathbf{n}_u \sim \mathcal{CN}(\mathbf{0}, \sigma^2 \mathbf{I})$  is the AWGN at the Rx.

Based on the above signal model, the signal-to-interference-plus-noise ratio (SINR) for the  $k^{\text{th}}$  DL user and the SINR at the FD BS for the  $i^{\text{th}}$  UL user are given as

$$\gamma_{d,k} = \frac{\left| \tilde{\mathbf{h}}_{d,k}^\top \mathbf{p}_k \right|^2}{\sum_{j \in \mathcal{G}_{d,p}, j \neq k} \left| \tilde{\mathbf{h}}_{d,k}^\top \mathbf{p}_j \right|^2 + \sigma^2}, \quad (12)$$

$$\gamma_{u,i} = \frac{P_u \left| \mathbf{w}_i^H \tilde{\mathbf{h}}_{u,i} \right|^2}{I_u(\mathbf{P}, \mathbf{W}, \Phi) + \|\mathbf{w}_i\|_F^2 \sigma^2}, \quad (13)$$

where the interference power term regarding the UL transmissions is given by

$$I_u(\mathbf{P}, \mathbf{W}, \Phi) = P_u \sum_{v \in \mathcal{G}_{u,q}, v \neq i} \left| \mathbf{w}_i^H \tilde{\mathbf{h}}_{u,v} \right|^2 + \sum_{k \in \mathcal{G}_{d,p}} \left| \mathbf{w}_i^H \mathbf{H}_{\text{SI}} \mathbf{p}_k + \mathbf{w}_i^H \mathbf{G}_u^\top \Phi \mathbf{G}_d \mathbf{p}_k \right|^2. \quad (14)$$

### III. PROBLEM FORMULATION AND SOLUTION

#### A. Weighted DL and UL Sum-rate Maximization over Time

We aim to maximize the weighted DL and UL sum-rate in the NR-BD-RIS-assisted FD LEO system over the entire scheduling period  $L$ . In the  $\ell^{\text{th}}$  time slot, the system serves  $p^{\text{th}}$  group of DL devices and  $q^{\text{th}}$  group of UL device. Specifically, we optimize the precoding matrix  $\mathbf{P}$ , combining matrix  $\mathbf{W}$ , and scattering matrix  $\Phi$ . The objective function is defined by:

$$f_o(\Phi) \triangleq \alpha_d \sum_{p \in \mathcal{L}} \sum_{i \in \mathcal{G}_{d,p}} \log_2(1 + \gamma_{d,k}) + \alpha_u \sum_{q \in \mathcal{L}} \sum_{j \in \mathcal{G}_{u,q}} \log_2(1 + \gamma_{u,i}), \quad (15)$$

where  $\alpha_d$  and  $\alpha_u$  represent the priorities assigned to DL and UL communications, respectively, with  $\alpha_d + \alpha_u = 1$ . Therefore, we have

$$\mathcal{P}1 : \max_{\mathbf{P}, \mathbf{W}, \Phi} f_o(\mathbf{P}, \mathbf{W}, \Phi) \quad (16a)$$

$$\text{s.t.} \quad \|\mathbf{P}\|_F^2 \leq P_d, \quad (16b)$$

$$\|\mathbf{W}\|_F^2 = 1, \quad (16c)$$

$$\Phi \in \mathcal{R}_i, i \in \{1, 2\}, \quad (16d)$$

$$\Phi \in \mathcal{S}_\ell, \ell \in \{1, 2, 3\}. \quad (16e)$$

Constraint (16d) enforces symmetry for the scattering matrix in the case of R-BD-RIS, i.e.,  $\Phi \in \mathcal{R}_1 = \{\Phi | \Phi = \Phi^\top\}$ , and asymmetry for NR-BD-RIS, i.e.,  $\Phi \in \mathcal{R}_2 = \{\Phi | \Phi \neq \Phi^\top\}$ . Constraint (16e) guarantees the impedance network remains lossless [6], [14], with  $\Phi$  satisfying: *i*)  $\mathcal{S}_1 = \{\Phi = \text{diag}(\phi_1, \dots, \phi_M) | |\phi_m| = 1, \forall m \in \mathcal{M}\}$  for D-RIS, *ii*)  $\mathcal{S}_2 = \{\Phi = \text{blkdiag}(\Phi_1, \dots, \Phi_G) | \Phi_g^H \Phi_g = \mathbf{I}, \forall g \in \mathcal{G}\}$  for GC-BD-RIS, and *iii*)  $\mathcal{S}_3 = \{\Phi | \Phi^H \Phi = \mathbf{I}\}$  for fully-connected BD-RIS. Since  $\mathcal{P}1$  involves a non-convex objective function with a logarithmic term and fractional structure, along with challenging constraints, a fractional programming approach [36] is adopted to address it.

#### B. Problem Transformation

We reformulate the problem  $\mathcal{P}1$  to a more manageable form using fractional programming, which involves two key steps: the Lagrangian dual transformation and the quadratic transformation [36]. As a result,  $\mathcal{P}1$  is transformed into

$$\mathcal{P}2 : \max_{\substack{\mathbf{P}, \mathbf{W}, \Phi \\ \boldsymbol{\iota}, \boldsymbol{\tau}}} f_\tau(\mathbf{P}, \mathbf{W}, \Phi, \boldsymbol{\iota}, \boldsymbol{\tau}) \quad (18a)$$

$$\text{s.t.} \quad (16b), (16c), (16d), \text{ and } (16e) \quad (18b)$$

where  $f_\tau(\Phi, \boldsymbol{\iota}, \boldsymbol{\tau})$  is defined in (17). Here,  $\boldsymbol{\iota} \triangleq [\boldsymbol{\iota}_d^\top, \boldsymbol{\iota}_u^\top]^\top = [\iota_{d,1}, \dots, \iota_{d,K}, \iota_{u,1}, \dots, \iota_{u,I}]^\top \in \mathbb{R}^{K+I}$  and  $\boldsymbol{\tau} \triangleq [\boldsymbol{\tau}_d^\top, \boldsymbol{\tau}_u^\top]^\top = [\tau_{d,1}, \dots, \tau_{d,K}, \tau_{u,1}, \dots, \tau_{u,I}]^\top \in \mathbb{R}^{K+I}$  are introduced auxiliary variables. To address the constraint for unitarity, the problem is reformulated using the PDD method. The resulting multi-variable optimization is then solved iteratively under the BCD framework, where each variable is updated sequentially until the objective function stabilizes.

The closed-form solutions of the auxiliary vectors  $\boldsymbol{\iota}$  and  $\boldsymbol{\tau}$  are derived in [25], [36]. Specifically, the optimal solution of  $\boldsymbol{\iota}$  is  $\boldsymbol{\iota}_{d,i}^{\text{opt}} = \gamma_{d,i}$  and  $\boldsymbol{\iota}_{u,j}^{\text{opt}} = \gamma_{u,j}$ . In addition,  $\boldsymbol{\tau}$  has the optimal solution given below

$$\tau_{d,k}^{\text{opt}} = \frac{\sqrt{1 + \iota_{d,k} \tilde{\mathbf{h}}_{d,k}^\top \mathbf{p}_k}}{\sum_{j \in \mathcal{G}_{d,p}} \left| \tilde{\mathbf{h}}_{d,k}^\top \mathbf{p}_j \right|^2 + \sigma^2}, \quad (19)$$

$$\tau_{u,i}^{\text{opt}} = \frac{\sqrt{(1 + \iota_{u,i}) \sqrt{P_u} \mathbf{w}_i^H \tilde{\mathbf{h}}_{u,i}}}{I_u(\mathbf{P}, \mathbf{W}, \Phi) + P_u \|\mathbf{w}_i\|_F^2 + \|\mathbf{w}_i\|_F^2 \sigma^2}. \quad (20)$$

$$\begin{aligned}
f_\tau(\mathbf{P}, \mathbf{W}, \Phi, \iota, \tau) = & \alpha_d \sum_{p \in \mathcal{L}} \sum_{k \in \mathcal{G}_{d,p}} \left( \log_2(1 + \iota_{d,k}) - \iota_{d,k} + 2\sqrt{1 + \iota_{d,k}} \Re \left\{ \tau_{d,k}^* \tilde{\mathbf{h}}_{d,k}^\top \mathbf{p}_k \right\} - |\tau_{d,k}|^2 \left( \sum_{j \in \mathcal{G}_{d,p}} \left| \tilde{\mathbf{h}}_{d,k}^\top \mathbf{p}_j \right|^2 + \sigma^2 \right) \right) \\
& + \alpha_u \sum_{q \in \mathcal{L}} \sum_{i \in \mathcal{G}_{u,q}} \left( \log_2(1 + \iota_{u,i}) - \iota_{u,i} + 2\sqrt{(1 + \iota_{u,i}) P_u} \Re \left\{ \tau_{u,i}^* \mathbf{w}_i^H \tilde{\mathbf{h}}_{u,i} \right\} - |\tau_{u,i}|^2 (I_u(\mathbf{P}, \mathbf{W}, \Phi) + P_u |\mathbf{w}_i^H \tilde{\mathbf{h}}_{u,i}|^2 + \sigma^2) \right),
\end{aligned} \tag{17}$$

**Algorithm 1:** Proposed Algorithm for FD LEO DL and UL Sum-rates over Time Design

---

**Input:**  $\tilde{\mathbf{H}}_d, \tilde{\mathbf{H}}_u, \mathbf{H}_{SI}, \mathbf{G}_d, \mathbf{G}_u$ .  
**Output:**  $\Phi^{\text{opt}}, \mathbf{P}^{\text{opt}}, \mathbf{W}^{\text{opt}}$ .

- 1 Initialize  $\Phi, \mathbf{P}, \mathbf{W}, t = 1$ .
- 2 **while** no convergence of objective function (18a) &  $t < t_{\text{max}}$  **do**
- 3     Update  $\iota_d^{\text{opt}}$  and  $\iota_u^{\text{opt}}$  by (12) and (13), respectively.
- 4     Update  $\tau_d^{\text{opt}}$  and  $\tau_u^{\text{opt}}$  by (19) and (20), respectively.
- 5     Update  $\mathbf{P}^{\text{opt}}$  by (24).
- 6     Update  $\mathbf{W}^{\text{opt}}$  by (27).
- 7     Update  $\Phi^{\text{opt}}$  by Algorithm 2.
- 8      $t = t + 1$ .
- 9 **end**
- 10 Return  $\Phi^{\text{opt}}, \mathbf{P}^{\text{opt}}, \mathbf{W}^{\text{opt}}$ .

---

**Transmit Precoder: Block  $\mathbf{P}$ .** Given that  $\mathbf{W}, \Phi, \iota$ , and  $\tau$  are fixed, we isolate the components associated with  $\mathbf{P}$

$$\begin{aligned}
f_\tau(\mathbf{P}) = & \alpha_d \sum_{p \in \mathcal{L}} \sum_{k \in \mathcal{G}_{d,p}} \left( 2\sqrt{1 + \iota_{d,k}} \Re \left\{ \tau_{d,k}^* \tilde{\mathbf{h}}_{d,k}^\top \mathbf{p}_k \right\} \right. \\
& \left. - \mathbf{p}_k^H \left( \sum_{w \in \mathcal{G}_{d,p}} |\tau_{d,k}|^2 \tilde{\mathbf{h}}_{d,w}^* \tilde{\mathbf{h}}_{d,w}^\top \right) \mathbf{p}_k \right) - \alpha_u \left( \sum_{q \in \mathcal{L}} \sum_{i \in \mathcal{G}_{u,q}} |\tau_{u,i}|^2 \right. \\
& \left. \sum_{k \in \mathcal{G}_{d,p}} |\mathbf{w}_i^H \mathbf{H}_{SI} \mathbf{p}_k + \mathbf{w}_i^H \mathbf{G}_u^\top \Phi \mathbf{G}_d \mathbf{p}_k|^2 \right).
\end{aligned} \tag{21}$$

Thus, we have the following subproblem

$$\mathcal{P}3 : \max_{\mathbf{P}} f_\tau(\mathbf{P}) \tag{22a}$$

$$\text{s.t. } \|\mathbf{P}\|_F^2 \leq P_d. \tag{22b}$$

Since both the objective function (22a) and the constraint (22b) are convex, the Lagrange multiplier method based on the Karush–Kuhn–Tucker (KKT) conditions can be applied to find the optimal solution. By introducing a multiplier  $\mu$ , the Lagrangian function is formulated as

$$\mathcal{P}4 : \max_{\mathbf{P}} f_\tau(\mathbf{P}) - \mu(\|\mathbf{P}\|_F^2 - P_d). \tag{23a}$$

Taking the partial derivatives of the Lagrangian function w.r.t  $\mathbf{P}$  and  $\mu$ , and setting them to  $\mathbf{0}$ , yields the optimal solution for each precoder  $\mathbf{p}_k$ , as shown in (24). The optimal value of  $\mu$ , denoted as  $\mu^{\text{opt}}$ , can be determined using a bisection search.

**Receive Combiner: Block  $\mathbf{W}$ .** With fixed  $\mathbf{P}, \Phi, \iota$ , and  $\tau$ , we isolate the terms related to  $\mathbf{W}$  in (17):

$$\begin{aligned}
f_\tau(\mathbf{W}) = & \sum_{q \in \mathcal{L}} \sum_{i \in \mathcal{G}_{u,q}} \left( 2\sqrt{1 + \iota_{u,i}} \sqrt{P_u} \Re \left\{ \tau_{u,i}^* \mathbf{w}_i^H \tilde{\mathbf{h}}_{u,i} \right\} \right. \\
& - |\tau_{u,i}|^2 \left( P_u \sum_{v \in \mathcal{G}_{u,q}} |\mathbf{w}_i^H \tilde{\mathbf{h}}_{u,v}|^2 + \sum_{k \in \mathcal{G}_{d,p}} |\mathbf{w}_i^H \mathbf{H}_{SI} \mathbf{p}_k \right. \\
& \left. \left. + \mathbf{w}_i^H \mathbf{G}_u^\top \Phi \mathbf{G}_d \mathbf{p}_k|^2 + \|\mathbf{w}_i\|^2 \sigma^2 \right) \right).
\end{aligned} \tag{25}$$

We then have the sub-problem:

$$\mathcal{P}5 : \max_{\mathbf{W}} f_\tau(\mathbf{W}) \tag{26a}$$

$$\text{s.t. } \|\mathbf{W}\|_F^2 = 1. \tag{26b}$$

Although the constraint (26b) is non-convex, we first treat this sub-problem as an unconstrained complex optimization problem. After convergence, the solution is normalized to satisfy the constraint. The optimal solution for each combiner  $\mathbf{w}_i$  is derived by setting  $\frac{\partial f_\tau(\mathbf{W})}{\partial \mathbf{w}_i} = \mathbf{0}$ :

$$\mathbf{w}_i^{\text{opt}} = (|\tau_{u,i}|^2 \zeta)^{-1} (\sqrt{1 + \iota_{u,i}} \sqrt{P_u} \tau_{u,i}^* \tilde{\mathbf{h}}_{u,i}), \forall i \in \mathcal{I}, \tag{27}$$

where  $\zeta$  is defined as:

$$\begin{aligned}
\zeta = & P_u \sum_{v \in \mathcal{G}_{u,q}} \tilde{\mathbf{h}}_{u,v} \tilde{\mathbf{h}}_{u,v}^H + \mathbf{H}_{SI} \sum_{k \in \mathcal{G}_{d,p}} \mathbf{p}_k \mathbf{p}_k^H \mathbf{H}_{SI}^H \\
& + \mathbf{G}_u^\top \Phi \mathbf{G}_d \sum_{k \in \mathcal{G}_{d,p}} \mathbf{p}_k \mathbf{p}_k^H \mathbf{G}_d^H \Phi^H \mathbf{G}_u^* \\
& + 2\Re \left\{ \mathbf{G}_u^\top \Phi \mathbf{G}_d \sum_{k \in \mathcal{G}_{d,p}} \mathbf{p}_k \mathbf{p}_k^H \mathbf{H}_{SI}^H \right\} + \sigma^2.
\end{aligned} \tag{28}$$

Finally,  $\mathbf{W}$  is normalized (i.e.,  $\mathbf{W}/\|\mathbf{W}\|_F$ ) to satisfy the receiver-side power constraint.

**BD-RIS Scattering Matrix:  $\Phi$ .** To update the scattering matrix  $\Phi$ , there are two challenges: 1) the coupling between the constraints (16d) and (16e); 2) the constraint for symmetry, i.e., (16d). To address the first challenge, the PDD method is adopted to decouple the constraints. Subsequently, the second challenge is addressed by linear reformulation of the scattering matrix. The details are given as follows.

We first isolate the terms w.r.t  $\Phi$  with fixed  $\mathbf{P}, \mathbf{W}, \iota$ , and  $\tau$  given in (29). We then employ a two-loop PDD method, introducing a replica  $\Psi$  of  $\Phi$  to decouple constraints (16d) and (16e), while adding the equality constraint  $\Phi = \Psi$ . An augmented Lagrangian problem  $\mathcal{P}3$  is formulated by incorporating the equality constraint into the objective function using

$$\mathbf{p}_k^{\text{opt}} = \left( \alpha_d \sum_{w \in \mathcal{G}_{d,p}} |\tau_{d,k}|^2 \tilde{\mathbf{h}}_{d,w}^* \tilde{\mathbf{h}}_{d,w}^\top + \alpha_u \left( \sum_{i \in \mathcal{G}_{u,q}} |\tau_{u,i}|^2 ((\mathbf{H}_{\text{SI}} \mathbf{w}_i \mathbf{w}_i^\top \mathbf{H}_{\text{SI}}) + 2\Re \{ \mathbf{H}_{\text{SI}}^H \mathbf{w}_i \mathbf{w}_i^\top \mathbf{G}_u^\top \Phi \mathbf{G}_d \}) \right. \right. \\ \left. \left. + \mathbf{G}_d^H \Phi^H \mathbf{G}_u^* \mathbf{w}_i \mathbf{w}_i^\top \mathbf{G}_u^\top \Phi \mathbf{G}_d \right) \right) + \mu^{\text{opt}} \mathbf{I} \right)^{-1} \alpha_d \sqrt{1 + \iota_{d,k}} \tau_{d,k} \mathbf{h}_{d,k}^*, \quad k \in \mathcal{K}, \quad (24)$$

$$f_\tau(\Phi) = \alpha_d \sum_{p \in \mathcal{L}} \sum_{k \in \mathcal{G}_{d,p}} 2\sqrt{1 + \iota_{d,k}} \Re \{ \tau_{d,k}^* \mathbf{h}_{d,k}^\top \Phi \mathbf{G}_d \mathbf{p}_k \} + \alpha_u \sqrt{P_u} \sum_{q \in \mathcal{L}} \sum_{i \in \mathcal{G}_{u,q}} 2\sqrt{1 + \iota_{u,i}} \Re \{ \tau_{u,i}^* \mathbf{w}_i^\top \mathbf{G}_u^\top \Phi \mathbf{h}_{u,i} \} \\ - \alpha_d \sum_{p \in \mathcal{L}} \sum_{k \in \mathcal{G}_{d,p}} |\tau_{d,k}|^2 |\mathbf{h}_{d,k}^\top \mathbf{p}_j|^2 - \alpha_u \sum_{q \in \mathcal{L}} \sum_{i \in \mathcal{G}_{u,q}} |\tau_{u,i}|^2 \left( P_u \sum_{v \in \mathcal{G}_{u,q}} |\mathbf{w}_i^\top \mathbf{h}_{u,v}|^2 + \sum_{k \in \mathcal{G}_{d,p}} |\mathbf{w}_i^\top \mathbf{H}_{\text{SI}} \mathbf{p}_k + \mathbf{w}_i^\top \mathbf{G}_u^\top \Phi \mathbf{G}_d \mathbf{p}_k|^2 \right) \\ = 2\alpha_d \sum_{p \in \mathcal{L}} \Re \{ \text{Tr}(\mathbf{C}_1 \Phi) \} + 2\alpha_u \sqrt{P_u} \sum_{q \in \mathcal{L}} \Re \{ \text{Tr}(\mathbf{C}_2 \Phi) \} - \alpha_d \sum_{p \in \mathcal{L}} \text{Tr}(\mathbf{B}_1 \Phi \mathbf{A}_1 \Phi^H) - \alpha_u P_u \sum_{q \in \mathcal{L}} \text{Tr}(\mathbf{A}_2 \Phi \mathbf{B}_2 \Phi^H) \\ - \alpha_u \sum_{q \in \mathcal{L}} \text{Tr}(\mathbf{A}_2 \Phi \mathbf{A}_1 \Phi^H), \quad (29)$$

---

**Algorithm 2:** Algorithm for Updating BD-RIS Scattering Matrix  $\Phi$ 


---

**Input:**  $\mathbf{P}, \mathbf{W}, \iota, \tau, \tilde{\mathbf{H}}_d, \tilde{\mathbf{H}}_u, \mathbf{H}_{\text{SI}}, \mathbf{G}_d, \mathbf{G}_u$ .

1 Initialize  $\{\Phi_g\}, \{\Psi_g\}, \{\Lambda_g\}, \rho, t_{\text{inner}} = t_{\text{outer}} = 1$ .

2 **for**  $g \leftarrow 1$  **to**  $G$  **do**

3   **while**  $\|\Phi_g - \Psi_g\|_\infty > \epsilon$  **&**  $t_{\text{outer}} < t_{\text{outer max}}$  **do**

4     **while** no convergence of objective function (31a) **&**  $t_{\text{inner}} < t_{\text{inner max}}$  **do**

5       Update  $\Phi_g$  by (35).

6       Update  $\Psi_g$  by (39).

7        $t_{\text{inner}} = t_{\text{inner}} + 1$ .

8     **end**

9     **if**  $\|\Phi_g - \Psi_g\|_\infty < \epsilon$  **then**

10        $\Lambda_g = \Lambda_g + \rho^{-1}(\Phi_g - \Psi_g)$ .

11     **else**

12        $\rho = c\rho$ .

13     **end**

14      $t_{\text{outer}} = t_{\text{outer}} + 1$ .

15 **end**

16 **end**

17 **return**  $\Phi^{\text{opt}} = \text{blkdiag}(\Phi_1^{\text{opt}}, \dots, \Phi_G^{\text{opt}})$ .

---

a dual variable  $\Lambda$  and a penalty coefficient  $\rho^{-1}$ . The inner loop focuses on solving the augmented Lagrangian problem  $\mathcal{P}3$ , while the outer loop updates the dual variable  $\Lambda_g$  and the penalty coefficient  $\rho^{-1}$  as needed to ensure the equality constraint (30b) is satisfied.

Specifically, the sub-optimization problem after introducing the copy  $\Psi$  and equality constraint  $\Phi = \Psi$  is given by

$$\mathcal{P}3 : \max_{\Phi, \Psi} f_\tau(\Phi) \quad (30a)$$

$$\text{s.t.} \quad \Psi_g^H \Psi_g = \mathbf{I}, \quad \forall g \in \mathcal{G}, \quad (30b)$$

$$\Phi_g = \Psi_g, \quad \forall g \in \mathcal{G}, \quad (30c)$$

$$\Phi_g \in \mathcal{R}_i, \quad i \in \{1, 2\}, \quad \forall g \in \mathcal{G}. \quad (30d)$$

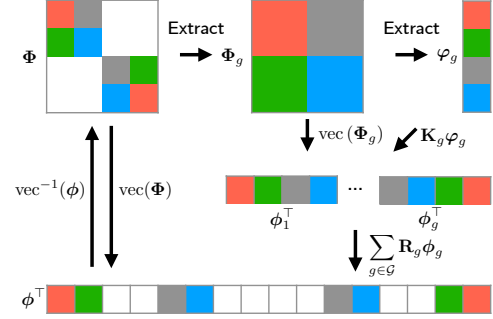


Fig. 4. An example of linear reformulation based on non-reciprocal case.

Then, the transformed augmented Lagrangian problem is:

$$\mathcal{P}4 : \min_{\Phi, \Psi} -f_\tau(\Phi) + \frac{1}{2\rho} \sum_{g \in \mathcal{G}} \|\Phi_g - \Psi_g\|^2 \quad (31a)$$

$$+ \sum_{g \in \mathcal{G}} \Re \{ \text{Tr}(\Lambda_g^H (\Phi_g - \Psi_g)) \}$$

$$\text{s.t.} \quad (30b), (30d).$$

Next, we adopt linear reformulation of the scattering matrix to address the constraint for symmetry (30d). The needed elements inside  $\Phi_g$  are extracted in a column by column order and vectorized as  $\varphi_g$ . Note that the need elements of NR-BD-RIS are all the elements in  $\Phi_g$ , while those of R-BD-RIS are the upper/lower triangular elements and the diagonal elements.

To recover the original matrix from the extracted vector  $\varphi_g$ , we introduce permutation matrix  $\mathbf{K}_g$  and mapping matrix  $\mathbf{R}_g$  in [25] and utilize them for the permutation process in (32) and mapping process in (33), respectively. An illustration of these processes with the non-reciprocal case is given in Fig. 4, where the vectorization is  $\psi_g \triangleq \text{vec}(\Psi_g)$ ,  $\lambda_g \triangleq \text{vec}(\Lambda_g)$ .

$$\phi_g \triangleq \text{vec}(\Phi_g) = \mathbf{K}_g \varphi_g, \quad \forall g \in \mathcal{G}. \quad (32)$$

$$\phi \triangleq \text{vec}(\Phi) = \sum_{g \in \mathcal{G}} \mathbf{R}_g \phi_g. \quad (33)$$

TABLE I  
NEWLY INTRODUCED NOTATIONS

$\mathbf{A}_1 = \sum_{j \in \mathcal{G}_{d,p}} \mathbf{G}_d \mathbf{p}_j \mathbf{p}_j^H \mathbf{G}_d^H$	$\mathbf{A}_2 = \sum_{i \in \mathcal{G}_{u,q}}  \tau_{u,i} ^2 \mathbf{G}_u^* \mathbf{w}_i \mathbf{w}_i^H \mathbf{G}_u^\top$
$\mathbf{B}_1 = \sum_{k \in \mathcal{G}_{d,p}}  \tau_{d,k} ^2 \mathbf{h}_{d,k}^* \mathbf{h}_{d,k}^\top$	$\mathbf{B}_2 = \sum_{v \in \mathcal{G}_{u,q}} \mathbf{h}_{u,v} \mathbf{h}_{u,v}^H$
$\mathbf{C}_1 = \sum_{k \in \mathcal{G}_{d,p}} \sqrt{1 + \iota_{d,k} \tau_{d,k}^*} \mathbf{G}_d \mathbf{p}_k \mathbf{h}_{d,k}^\top$	$\mathbf{C}_2 = \sum_{i \in \mathcal{G}_{u,q}} \sqrt{1 + \iota_{u,i} \tau_{u,i}^*} \mathbf{h}_{u,i} \mathbf{w}_i^H \mathbf{G}_u^\top$

Following the preprocessing step, the two-loop PDD method can be applied to solve the problem  $\mathcal{P}4$ .

1) *Update of  $\Phi_g$  in the Inner Loop:* The sub-problem w.r.t  $\Phi_g$  in the form of  $\varphi_g$  is written as

$$\mathcal{P}5 : \min_{\varphi_g} L(\varphi_g) = \varphi_g^H \Delta \varphi_g - 2\Re \{ \varphi_g^H \delta \}. \quad (34a)$$

Since  $\mathcal{P}5$  is an unconstrained quadratic optimization problem, the optimal solution is obtained by setting  $\frac{\partial L(\varphi_g)}{\partial \varphi_g} = \mathbf{0}$ . Therefore, the optimal solution of  $\varphi_g^{\text{opt}}$  is:

$$\varphi_g^{\text{opt}} = \Delta^{-1} \delta, \quad (35)$$

where  $\Delta$  and  $\delta$  are defined as

$$\begin{aligned} \Delta &= \alpha_u \mathbf{K}_g^H \mathbf{R}_g^H \sum_{q \in \mathcal{L}} (P_u \mathbf{B}_2^\top \otimes \mathbf{A}_2 + \mathbf{A}_1^\top \otimes \mathbf{A}_2) \mathbf{R}_g \mathbf{K}_g \\ &\quad + \alpha_d \mathbf{K}_g^H \mathbf{R}_g^H \sum_{p \in \mathcal{L}} (\mathbf{A}_1^\top \otimes \mathbf{B}_1) \mathbf{R}_g \mathbf{K}_g + \frac{1}{2\rho} \mathbf{K}_g^H \mathbf{K}_g, \\ \delta &= \alpha_d \mathbf{K}_g^H \mathbf{R}_g^H \sum_{p \in \mathcal{L}} \text{vec}^*(\mathbf{C}_1^\top) + \alpha_u \mathbf{K}_g^H \mathbf{R}_g^H \sum_{q \in \mathcal{L}} \sqrt{P_u} \text{vec}^*(\mathbf{C}_2^\top) \\ &\quad + \frac{1}{2\rho} \mathbf{K}_g^H \mathbf{K}_g \psi_g - \frac{1}{2} \mathbf{K}_g^H \lambda_g. \end{aligned} \quad (36)$$

The introduced expressions are listed in the Table I.

2) *Update of  $\Psi_g$  in the Inner Loop:* The optimization problem involving  $\Psi_g$  is an orthogonal procrustes problem and given by

$$\mathcal{P}5 : \min_{\Psi_g} \|\Psi_g - (\rho \Lambda_g + \Phi_g)\|_F^2, \quad (38a)$$

$$\text{s.t. } \Psi_g^H \Psi_g = \mathbf{I}. \quad (38b)$$

This problem has a closed-form solution given by [37]

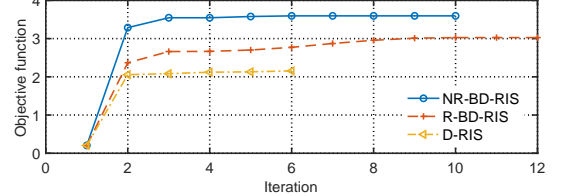
$$\Psi_g^{\text{opt}} = \mathbf{U}_g \mathbf{V}_g^H, \quad (39)$$

where the unitary matrices  $\mathbf{U}_g$  and  $\mathbf{V}_g$  are derived from the singular value decomposition (SVD) of  $\rho \Lambda_g + \Phi_g$ .

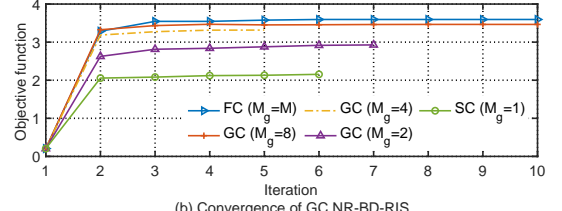
3) *Update of  $\Lambda_g$  and  $\rho$  in the Outer Loop:* Once the inner loop converges, the dual variable  $\Lambda_g$  and the penalty coefficient  $\rho$  are updated in the outer loop. The convergence criterion for the outer loop is defined as  $\|\Phi_g - \Psi_g\|_\infty < \epsilon$ , where  $\epsilon$  is a small positive threshold. This ensures that the equality constraint (30c) is satisfied. If the criterion is met, the dual variable is updated as

$$\Lambda_g = \Lambda_g + \rho^{-1} (\Phi_g - \Psi_g). \quad (40)$$

If  $\Phi_g$  and  $\Psi_g$  are not sufficiently close, the penalty coefficient is updated as  $\rho = c\rho$ ,  $c \in (0, 1)$ . Once the optimal solution for each group  $\Phi_g^{\text{opt}}$  is obtained, the overall scattering matrix  $\Phi^{\text{opt}}$  can be reconstructed. The procedure for updating the scattering matrix  $\Phi$  is outlined in Algorithm 2.



(a) Convergence of NR-BD-RIS, R-BD-RIS and D-RIS



(b) Convergence of GC NR-BD-RIS

Fig. 5. Convergence of the proposed algorithm. The Tx and Rx antenna are fixed at  $88^\circ$  and  $92^\circ$ , respectively. The RIS arrays with  $M = 16$  RIS elements are set to a UPA ( $4 \times 4$ ). The number of Tx and Rx antennas are both  $N = 2$ , and  $G_{d,p} = 2$  DL devices and  $G_{u,q} = 2$  UL devices are served at each time slot. The RIS is configured as a UPA ( $4 \times 4$ ) with  $M = 16$  elements, and the update frequency is set to  $L = 2$ . (a) Convergence for FC NR-BD-RIS, R-BD-RIS, and D-RIS. (b) Convergence for GC NR-BD-RIS with varying group sizes.

### C. Convergence Analysis

The convergence of the proposed algorithm is evaluated. The objective function (18a) is guaranteed to converge to at least a local optimum. Let  $v^t$  represent the objective function value at the  $t^{\text{th}}$  iteration. In Algorithm 1, the blocks are updated through an iterative procedure. For each group  $g \in \mathcal{G}$ , the PDD step used to update  $\Phi_g$  converges within its inner loop, since the related sub-problems are convex and have unique solutions. The outer loop of the PDD method converges to a KKT point as the augmented Lagrangian enforces constraint satisfaction while updating the dual variables [38]. As a result,  $\Phi$  converges to a local optimum. Similarly, the optimization of  $\iota$ ,  $\tau$ ,  $\mathbf{P}$ , and  $\mathbf{W}$  is convex, ensuring that the objective function (18a) is monotonically non-decreasing, i.e.,  $v^t \geq v^{t-1}$ . Therefore, the overall algorithm converges to a local optimum.

Simulation results in Fig. 5 (a) confirm the convergence of Algorithm 1 for fully-connected NR-BD-RIS, R-BD-RIS, and D-RIS, with all cases converging within 12 iterations. The NR-BD-RIS achieves the highest objective value, highlighting its superior performance. Fig. 5 (b) shows the convergence for GC-NR-BD-RIS, where smaller group sizes  $M_g$  lead to lower objective values due to reduced flexibility in the scattering matrix design.

### D. Complexity Analysis

In the BCD framework, each block is optimized iteratively. The update of  $\iota$  and  $\tau$  has a per-iteration cost of  $\mathcal{O}(K^2 M^2)$ , since it mainly consists of element-wise computations and matrix–vector products. The design of precoder  $\mathbf{P}$  involves matrix inversion together with a bisection search, giving a complexity of  $\mathcal{O}(K(M^2 + I_b N^3))$ , where  $I_b$  denotes the number of bisection steps. The combiner  $\mathbf{W}$  update also relies on matrix inversion and incurs a cost of  $\mathcal{O}(KN^3)$ .

Among all blocks, the PDD update of  $\Phi$  requires the largest computational effort. Specifically, the Kronecker product in (35) contributes  $\mathcal{O}(M_g^2 M^4)$ , while the SVD operation in (39) adds  $\mathcal{O}(M_g^3)$ . Consequently, the complexity of Algorithm 2 is  $\mathcal{O}(GI_{\text{outer}} I_{\text{inner}} M_g^2 M^4)$ , where  $I_{\text{outer}}$  and  $I_{\text{inner}}$  denote the outer and inner iteration counts in the PDD method, respectively. Overall, the total complexity of the proposed algorithm is  $\mathcal{O}(I_{\text{BCD}}(K^2 M^2 + K(M^2 + I_b N^3) + K N^3 + GI_{\text{outer}} I_{\text{inner}} M_g^2 M^4))$ , where  $I_{\text{BCD}}$  represents the number of BCD iterations needed to reach convergence.

#### IV. NUMERICAL EVALUATION

This section assesses the performance of the proposed NR-BD-RIS-assisted FD LEO satellite system and compares its DL and UL sum-rates with those of the R-BD-RIS and D-RIS, showing the benefit of the NR-BD-RIS. Specifically, in the SU case, we analyze the impact of the following parameters on the DL and UL sum-rate performance: 1) angles of ground UL devices, 2) angular separation between the Tx and Rx antennas, 3) RIS update frequency, 4) sum-rate region by varying DL and UL weights, 5) number of RIS elements, 6) group size of the GC NR-BD-RIS, 7) SI power level, and 8) number of DL and UL devices. Additionally, in the MU case, we assess the performance by examining the impact of RIS update frequency and the sum-rate region for different numbers of DL and UL devices.

In the simulation, we consider both SU case (i.e.,  $G_{d,p} = 1, G_{u,q} = 1$ ) and MU cases (i.e.,  $G_{d,p} > 1, G_{u,q} > 1$ ) within each time slot. Since the LoS links are common in satellite communications, we model the far-field channel between the RIS and ground DL/UL devices using a Rician factor  $\kappa = 10$  dB. The DL and UL priority parameters are set equally, i.e.,  $\alpha_d = \alpha_u = 0.5$ . To suppress the power level of SI, the Tx and Rx antennas are positioned at  $90 \pm \Delta_{\text{deg}}$ , where  $\Delta_{\text{deg}}$  is a small angular deviation from  $90^\circ$ . Specifically, the Tx and Rx antennas are fixed at  $88^\circ$  and  $92^\circ$ , respectively, ensuring that the incident wave from the Tx antenna to the RIS is nearly orthogonal to the RIS plane (yz plane). This configuration maximizes the normalized power radiation pattern in (7). Since the Tx and Rx antennas are close to the RIS, the loop interference is treated as reflected SI. We assume that the total SI is pre-suppressed using SI cancellation techniques, such as those in the digital domain [35], and is set to 20 dB larger than the noise floor. Additionally, we consider fully-connected NR-BD-RIS and R-BD-RIS. The simulation parameters, particularly those relevant to the LEO satellite, are summarized in Table II.

##### A. Single-user (SU) Case

###### 1) DL and UL Sum-rate versus the location of UL User:

To observe the sum-rate performance of NR-BD-RIS-assisted FD LEO satellite communication system, we first evaluate the DL and UL sum-rate versus the angle of the UL device. The RIS array is set to a UPA. In addition, the DL device is fixed at  $60^\circ$ . The UL device is varied from  $30^\circ$  to  $150^\circ$ , this is decided by the height of the satellite and the radius of the Earth. Fig. 6 presents the results. The round shape is due to

TABLE II  
SIMULATION PARAMETERS

Parameters	Value
Transmit budget $P_t$	50 dBm
Noise power spectral density	-174 dBm/Hz
Carrier frequency $f_c$	10.5 GHz (K band)
Satellite height $d_{\text{sat}}$	600 km
Bandwidth $B$	1 MHz
Pathloss coefficient $\eta$	2
Distance between the Tx antenna and the RIS $r_{tx}$	5 m
Antenna gain for the Tx and Rx $G_t, G_r$	30, 33.4 dB
Rainfall rate	31.119

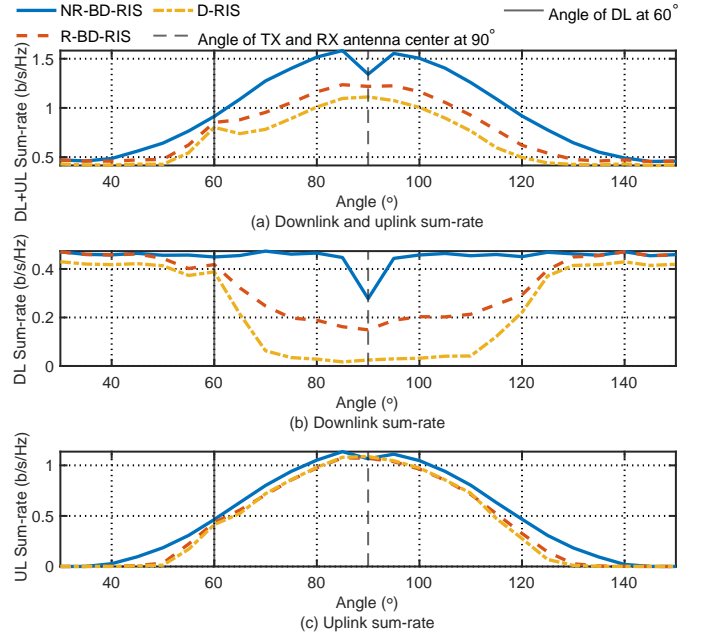


Fig. 6. Comparison of DL and UL sum-rates for NR-BD-RIS, R-BD-RIS, and D-RIS as a function of the UL device angle. The Tx and Rx antennas are positioned at  $88^\circ$  and  $92^\circ$ , respectively, while the DL device is fixed at  $60^\circ$ . The RIS is configured as a UPA with  $M = 16$  elements ( $4 \times 4$ ).

that the Earth surface is not flat, thus the pathloss at the edges (i.e.,  $30^\circ$  and  $150^\circ$ ) is large. The results show that NR-BD-RIS performs better than both R-BD-RIS and D-RIS when the UL device is not aligned with the DL device. The reason of the performance gap is that the NR-BD-RIS breaks the channel reciprocity [25], thus multiple impinging and reflected directions can be supported. When UL device is aligned with DL device, i.e.,  $60^\circ$ , there are just two impinging and reflected directions, thus other two types of RIS can tackle with. In addition, when the angle of UL device is aligned with the Tx antenna at the LEO satellite, there is a deterioration of all the three RISs. This is because that it is difficult for the receive antenna at the LEO satellite to distinguish the signals, and the interference is severe.

2) *The Impact of the Separation of Tx and Rx:* The spacing between the Tx and Rx antennas on the LEO satellite can reduce SI in the propagation domain [39]. To determine how large this spacing can be, we study the DL and UL sum-rates as a function of the angular separation between the Tx and Rx antennas, denoted as  $2\Delta_{\text{deg}}$ . Specifically, the Tx antenna

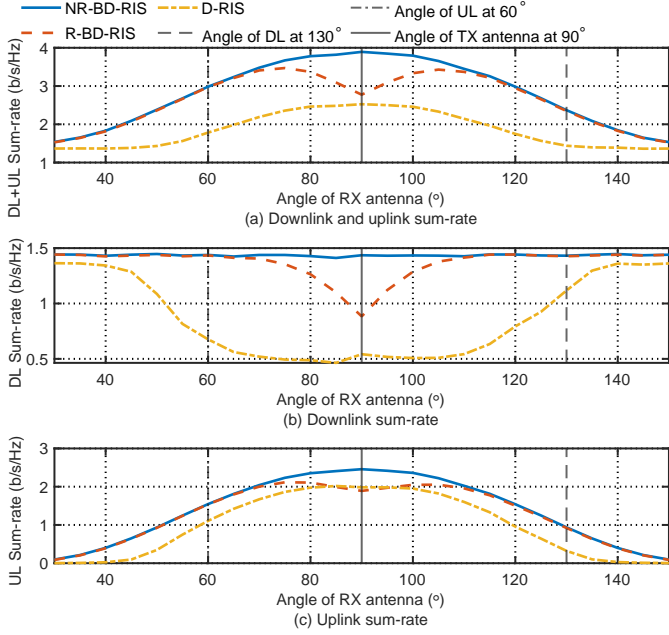


Fig. 7. Comparison of DL and UL sum-rates for NR-BD-RIS, R-BD-RIS, and D-RIS as a function of the UL device angle. The RIS is configured as a UPA with  $M = 16$  elements ( $4 \times 4$ ). The Tx antenna is fixed at  $90^\circ$ .

is fixed at  $90^\circ$ , while the Rx antenna is varied from  $30^\circ$  to  $150^\circ$ . The results show that when the separation is within  $15^\circ$ , the NR-BD-RIS consistently outperforms the R-BD-RIS and D-RIS. This is because the high channel correlation of the DL and UL channels between the RIS and Tx/Rx antennas allows the NR-BD-RIS to effectively maximize the DL and UL sum-rates simultaneously. For separations greater than  $15^\circ$ , the performance of the NR-BD-RIS is the same as that of the R-BD-RIS, both of which outperform the D-RIS. This comes from the interconnected impedance structure of the BD-RIS, which provides more control than the single-connected impedance in the D-RIS and thus leads to better performance. Hence, to limit SI while preserving the gain of NR-BD-RIS, the Tx and Rx antenna separation should stay within  $15^\circ$  for this configuration.

3) *The Impact of Update Frequency of NR-BD-RIS:* To alleviate the burden of real-time updates to the scattering matrix, we evaluate the impact of the RIS update frequency on the average DL and UL sum-rate over  $L$  time slots. The update frequency denotes the number of consecutive time slots over which the same RIS configuration is reused. An update frequency of 1 implies that the RIS is reconfigured at every time slot, whereas a frequency of  $\ell$  indicates that the RIS is optimized once and applied to  $\ell$  successive DL/UL user groups. Specifically, we optimize the scattering matrix by solving  $\mathcal{P}1$ , assuming that the locations of all users in the  $L$  time slots are known during optimization. The average DL and UL sum-rate per time slot is then calculated. The locations of the DL and UL devices are randomly selected within the range  $[30^\circ, 150^\circ]$ .

The results in Fig. 8 show that the NR-BD-RIS always achieves higher performance than the R-BD-RIS and D-RIS, regardless of the RIS update frequency. Notably, the

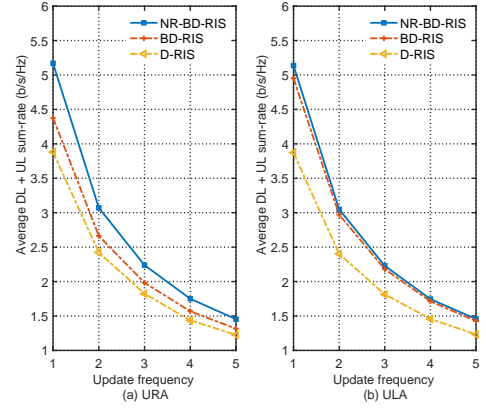


Fig. 8. Average DL and UL sum-rate of NR-BD-RIS, R-BD-RIS, and D-RIS. The locations of the Tx and Rx antenna are fixed at  $88^\circ$ , and  $92^\circ$ . The locations of the DL and UL devices are randomly selected from  $[30^\circ, 150^\circ]$ . The RIS arrays with  $M = 32$  RIS elements are set to (a) URA ( $4 \times 8$ ), (b) ULA ( $1 \times 32$ ).

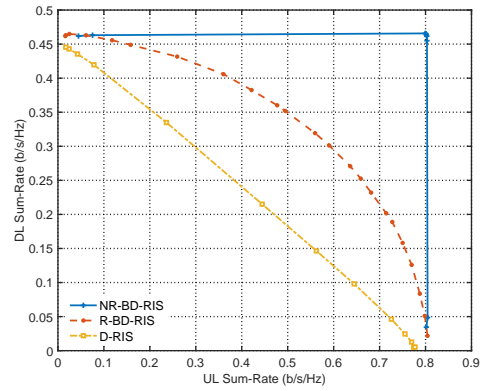


Fig. 9. The sum-rate regions for NR-BD-RIS, R-BD-RIS, and D-RIS with  $L = 1$ . The locations of the Tx and Rx antenna are fixed at  $88^\circ$ , and  $92^\circ$ . The locations of the DL and UL devices are located at  $60^\circ$  and  $110^\circ$ , respectively. The RIS with  $M = 16$  RIS elements is set to a UPA ( $4 \times 4$ ).

performance gap remains even when the RIS is updated less frequently, i.e.,  $L = 5$ . This highlights the NR-BD-RIS's ability to effectively support devices at varying locations over multiple time slots. This is because of its internal non-reciprocal impedance network. This capability significantly reduces the need for real-time reconfiguration, enhancing its practicality for implementation. In contrast, other two types of RIS show limited flexibility in serving devices over multiple time slots. Thus, they require a higher update frequency to achieve performance comparable to the NR-BD-RIS.

4) *Sum-rate Region:* By varying the DL and UL priority parameters  $\alpha_d$  and  $\alpha_u$ , we can obtain the sum-rate region for the NR-BD-RIS, R-BD-RIS, and D-RIS in Fig. 9. The NR-BD-RIS yields a much larger sum-rate region than the R-BD-RIS and D-RIS, especially when both DL and UL transmissions are considered. This is because the NR-BD-RIS can break channel reciprocity, allowing it to optimally and simultaneously maximize both DL and UL rates. Since the NR-BD-RIS can better tackle with the loop interference and SI, it can achieve true FD operation without a trade-off between DL and UL. When the priority is solely on

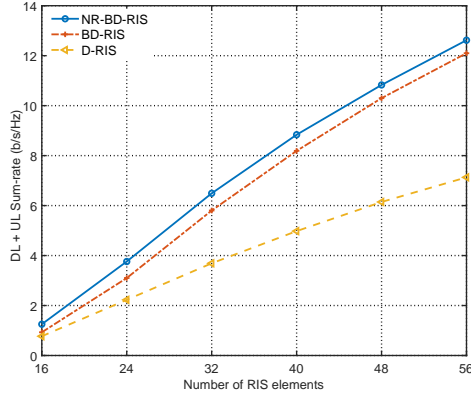


Fig. 10. The DL and UL sum-rate of NR-BD-RIS, R-BD-RIS, and D-RIS versus the number of RIS element with  $L = 1$ . The RIS is set to a UPA with fixed 2 rows. The locations of the Tx and Rx antenna are fixed at  $88^\circ$ , and  $92^\circ$ . The locations of the DL and UL devices are located at  $60^\circ$  and  $110^\circ$ , respectively.

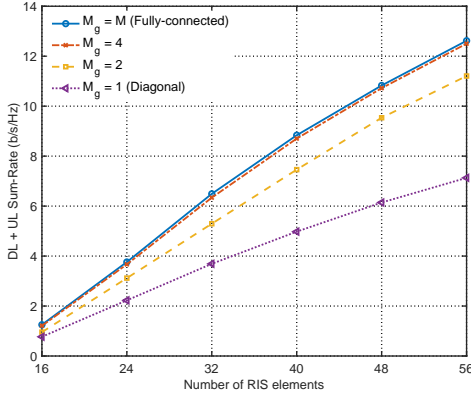


Fig. 11. The DL and UL sum-rate of NR-BD-RIS versus the number of group size with  $L = 1$ . The RIS is set to a UPA with fixed 2 rows. The locations of the Tx and Rx antenna are fixed at  $88^\circ$ , and  $92^\circ$ . The locations of the DL and UL devices are located at  $60^\circ$  and  $110^\circ$ , respectively.

DL or UL, NR-BD-RIS has no gain over R-BD-RIS, as both can effectively maximize the rate in a single direction. However, both outperform the D-RIS due to the interconnected impedance network of the BD-RIS.

5) *The Impact of the Number of RIS Elements*: To assess how the number of RIS elements affects the DL and UL sum-rate, we analyze the performance as the number of RIS elements increases. As illustrated in Fig. 10, the NR-BD-RIS consistently outperforms both the R-BD-RIS and D-RIS. This advantage arises from the NR-BD-RIS's ability to break channel reciprocity, allowing it to handle multiple impinging and reflected directions for both DL and UL devices. In contrast, other two types of RIS are limited by channel reciprocity, which restricts their performance capabilities.

6) *The Impact of the Number of Group Size*: We evaluate the impact of group size on the DL and UL sum-rate for the NR-BD-RIS, R-BD-RIS, and D-RIS. The RIS is divided into  $G$  groups, each containing  $M_g$  elements, such that  $M = GM_g$ . The group size  $M_g$  is varied with a fixed total number of RIS elements  $M = 56$ . When  $M_g = 1$ , it corresponds to the single-connected case, while  $M_g = M$  represents the fully-connected case. The results are shown in Fig. 11 and

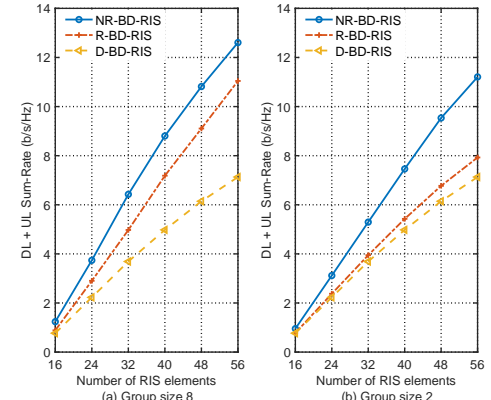


Fig. 12. The DL and UL sum-rate of NR-BD-RIS, R-BD-RIS, and D-RIS with  $L = 1$  when (a) group size  $M_g = 8$  and (b) group size  $M_g = 2$ . The RIS is set to a UPA with fixed 2 rows. The locations of the Tx and Rx antenna are fixed at  $88^\circ$ , and  $92^\circ$ . The locations of the DL and UL devices are located at  $60^\circ$  and  $110^\circ$ , respectively.

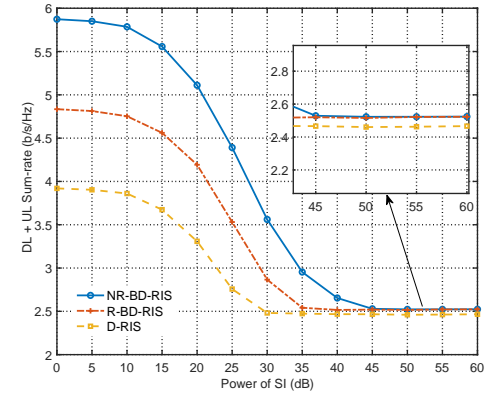


Fig. 13. The DL and UL sum-rate of NR-BD-RIS, R-BD-RIS, and D-RIS versus the number of DL and UL users with  $L = 1$ . The locations of the DL and UL devices are located at  $60^\circ$  and  $110^\circ$ , respectively. The RIS arrays with  $M = 16$  RIS elements are set to a ULA ( $1 \times 16$ ).

Fig. 12. The DL and UL sum-rate increases with the group size for all three RIS types. This is because a larger group size provides more flexibility in controlling the scattering matrix, thereby enhancing performance. Importantly, the NR-BD-RIS consistently achieves better performance than both the R-BD-RIS and D-RIS for all group sizes. This superiority stems from the NR-BD-RIS's capability to break channel reciprocity, enabling it to efficiently handle multiple impinging and reflected directions for both DL and UL devices.

7) *The Impact of the Power of SI level*: We analyze the impact of SI power on the DL and UL sum-rates for the NR-BD-RIS, R-BD-RIS, and D-RIS, with the DL device and UL device located at  $60^\circ$  and  $110^\circ$ , respectively. The Tx/Rx antennas are configured with  $N = 1$ , and the RIS consists of  $M = 16$  elements. In Fig. 13, it is observed that the sum-rates decline as SI power increases due to the severe interference in the UL SINR (13). The NR-BD-RIS achieves the highest sum-rates; however, its advantage diminishes as SI power rises. At high SI levels, e.g., 45 dB, the UL rate becomes small, therefore, the DL and UL sum-rate is dominated by the DL rate. This explains why the curves become flat, which reflect

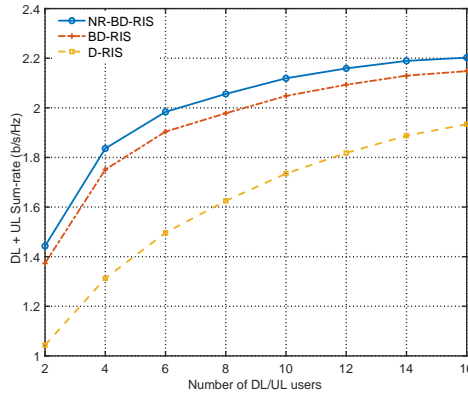


Fig. 14. The DL and UL sum-rate of NR-BD-RIS, R-BD-RIS, and D-RIS versus the number of DL and UL users with  $L = 1$ . The locations of the DL and UL devices are randomly selected from  $[30^\circ, 150^\circ]$ . The RIS arrays with  $M = 16$  RIS elements are set to a ULA ( $1 \times 16$ ).

the DL rates. As discussed in IV-A4, when focusing on one-directional transmission, NR-BD-RIS has benefit. Thus, the performances of NR-BD-RIS and R-BD-RIS are the same at high SI levels. The R-BD-RIS outperforms the D-RIS due to the interconnections inside the impedance network, enabling control over both amplitude and phase.

8) *The Impact of the Number of DL/UL users:* We analyze the impact of the number of DL and UL users on the DL and UL sum-rate for the NR-BD-RIS, R-BD-RIS, and D-RIS. The Tx/Rx antennas are configured with  $N = 1$ , and the RIS consists of  $M = 16$  elements. The DL and UL devices are randomly positioned within the range  $[30^\circ, 150^\circ]$ . In Fig. 14, the NR-BD-RIS consistently achieves higher performance compared to the R-BD-RIS and D-RIS for all user counts. While the DL and UL sum-rate increases with the number of users for all three RIS types, the rate of increase diminishes as the number of users grows due to heightened interference among users. The NR-BD-RIS's capability to break channel reciprocity enables it to efficiently handle the added complexity of serving multiple users, thereby sustaining its performance advantage over the other RIS types.

### B. Multiple-user (MU) Case

1) *The Impact of Update Frequency of NR-BD-RIS:* We analyze the impact of the RIS update frequency on the average DL and UL sum-rate over  $L$  time slots in a MU scenario. Each time slot accommodates  $G_{d,p} = 2$  DL devices and  $G_{u,q} = 2$  UL devices, with their positions randomly distributed within  $[30^\circ, 150^\circ]$ . The Tx and Rx antennas are configured with  $N = 2$ , and the RIS consists of  $M = 32$  elements. The results, presented in Fig. 15, indicate that the NR-BD-RIS consistently outperforms the R-BD-RIS and D-RIS, regardless of the RIS update frequency. The performance gap remains even when the RIS is updated less frequently, i.e.,  $L = 5$ . This shows the NR-BD-RIS's ability to effectively support multiple devices at varying locations over multiple time slots due to its non-reciprocal impedance network. This capability significantly reduces the need for real-time reconfiguration, enhancing its practicality for implementation.

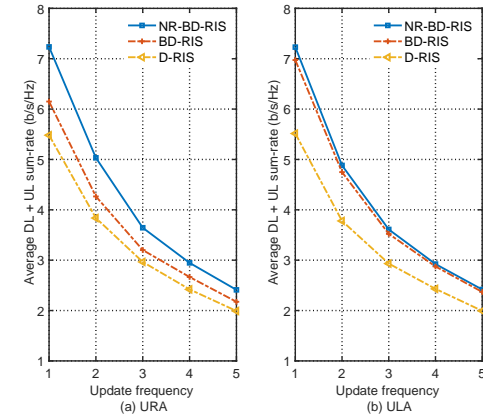


Fig. 15. Average DL and UL sum-rate of NR-BD-RIS, R-BD-RIS, and D-RIS versus the RIS update frequency  $L$ . The Tx and Rx antenna array are fixed at  $88^\circ$  and  $92^\circ$ , respectively. Each time slot serves  $G_{d,p} = 2$  DL devices and  $G_{u,q} = 2$  UL devices, with their locations randomly selected within  $[30^\circ, 150^\circ]$ . Both the Tx and Rx arrays have  $N = 2$  antennas. The RIS is configured as (a) UPA with  $M = 32$  elements ( $4 \times 8$ ), (b) ULA with  $M = 32$  elements ( $1 \times 32$ ).

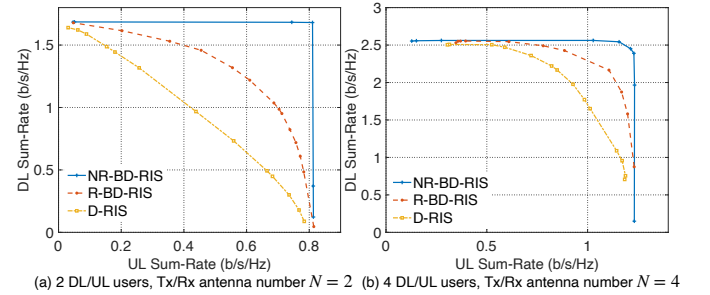


Fig. 16. Sum-rate regions for NR-BD-RIS, R-BD-RIS, and D-RIS with  $L = 1$ . The Tx and Rx antennas are fixed at  $88^\circ$  and  $92^\circ$ , respectively. The RIS has  $M = 16$  elements configured as a UPA ( $4 \times 4$ ). (a) Two DL devices at  $80^\circ$  and  $140^\circ$ , and two UL devices at  $40^\circ$  and  $110^\circ$ . (b) Four fixed DL and UL devices.

2) *Sum-rate Region:* The sum-rate regions for the NR-BD-RIS, R-BD-RIS, and D-RIS in a MU scenario are shown in Fig. 16. In Fig. 16(a), two DL devices are located at  $80^\circ$  and  $140^\circ$ , while two UL devices are at  $40^\circ$  and  $110^\circ$ . In Fig. 16(b), four fixed DL and UL devices are considered. The sum-rate region of the NR-BD-RIS is still larger than that of the R-BD-RIS and D-RIS in MU cases, especially when both DL and UL transmissions are considered. This is because the NR-BD-RIS can break channel reciprocity, allowing it to simultaneously maximize both DL and UL rates. When one direction transmission is considered, NR-BD-RIS has no gain over R-BD-RIS, as both can effectively maximize the rate in a single direction. However, both outperform the D-RIS due to the interconnected impedance network of the BD-RIS.

## V. CONCLUSION

This work has investigated the FD LEO satellite communication system enabled by NR-BD-RIS to achieve simultaneous DL and UL transmission. To serve a broader range of ground devices, we have considered a time-sharing scheduling framework. We have formulated the weighted DL and UL

sum-rate maximization problem over time. To solve the non-convex problem, we have designed an iterative algorithm using BCD and PDD methods. The numerical results have shown that the NR-BD-RIS outperforms the conventional R-BD-RIS and D-RIS, especially when the RIS is updated less frequently. In addition, the gain of NR-BD-RIS keeps even when the Tx and Rx antennas are not strictly aligned. In MU scenarios, the NR-BD-RIS demonstrates gains and performance in supporting multiple users with varying locations. We attribute these advantages to the NR-BD-RIS's ability to break channel reciprocity, enabling it to effectively control multiple impinging and reflected directions for both DL and UL devices. This work paves the way for future studies on NR-BD-RIS-enabled satellite communications.

## REFERENCES

- [1] M. Toka, B. Lee, J. Seong *et al.*, “RIS-empowered LEO satellite networks for 6G: Promising usage scenarios and future directions,” *IEEE Commun. Mag.*, vol. 62, no. 11, pp. 128–135, 2024.
- [2] K. Tekbiyik, G. K. Kurt, and H. Yanikomeroglu, “Energy-efficient RIS-assisted satellites for IoT networks,” *IEEE Internet Things J.*, vol. 9, no. 16, pp. 14 891–14 899, Aug. 2022.
- [3] E. Lagunas, T. Ramirez-Parracho, J. A. Vasquez-Peralvo *et al.*, “Full-duplex techniques for satellite communications: Feasibility analysis and roadmap,” *IEEE Open J. of the Comm. Society.*, 2025.
- [4] C. Huang, A. Zappone, G. C. Alexandropoulos *et al.*, “Reconfigurable intelligent surfaces for energy efficiency in wireless communication,” *IEEE Trans. Wireless Commun.*, vol. 18, no. 8, pp. 4157–4170, 2019.
- [5] S. Sekimori, Y. Kawamoto, N. Kato *et al.*, “Frequency prism in delay adjustable intelligent reflecting surfaces for long distance communications in LEO satellite networks,” in *Proc. IEEE Int. Conf. Commun. (ICC)*, Denver, USA, 2024, pp. 3470–3475.
- [6] S. Shen, B. Clerckx, and R. Murch, “Modeling and architecture design of reconfigurable intelligent surfaces using scattering parameter network analysis,” *IEEE Trans. Wireless Commun.*, vol. 21, no. 2, pp. 1229–1243, Feb. 2022.
- [7] H. Li, S. Shen, M. Nerini *et al.*, “Reconfigurable intelligent surfaces 2.0: Beyond diagonal phase shift matrices,” *IEEE Commun. Mag.*, vol. 62, no. 3, pp. 102–108, Mar. 2024.
- [8] H. Li, M. Nerini, S. Shen *et al.*, “A tutorial on beyond-diagonal reconfigurable intelligent surfaces: Modeling, architectures, system design and optimization, and applications,” *arXiv preprint arXiv:2505.16504*, 2025.
- [9] Z. Liu, Y. Liu, S. Shen *et al.*, “Enhancing ISAC network throughput using beyond diagonal RIS,” *IEEE Wireless Commun. Lett.*, vol. 13, no. 6, pp. 1670–1674, 2024.
- [10] M. Nerini, S. Shen, H. Li *et al.*, “Beyond diagonal reconfigurable intelligent surfaces utilizing graph theory: Modeling, architecture design, and optimization,” *IEEE Trans. Wireless Commun.*, 2024.
- [11] X. Zhou, T. Fang, and Y. Mao, “A novel Q-stem connected architecture for beyond-diagonal reconfigurable intelligent surfaces,” in *Proc. IEEE Int. Conf. Commun. (ICC)*, Montreal, Canada, 2025, pp. 6880–6885.
- [12] Z. Wu and B. Clerckx, “Beyond diagonal RIS in multiuser MIMO: Graph theoretic modeling and optimal architectures with low complexity,” *arXiv preprint arXiv:2502.16509*, 2025.
- [13] H. Li and B. Clerckx, “Non-reciprocal beyond diagonal RIS: Multiport network models and performance benefits in full-duplex systems,” *IEEE Trans. Commun.*, 2025.
- [14] D. M. Pozar, *Microwave engineering: Theory and techniques*. Hoboken, NJ, USA: Wiley, 2009.
- [15] J. Xu, H. Wang, R. Liu *et al.*, “Non-reciprocal reconfigurable intelligent surfaces,” *IEEE Wireless Commun. Lett.*, 2025.
- [16] Q. Li, M. El-Hajjar, I. Hemadah *et al.*, “Reconfigurable intelligent surfaces relying on non-diagonal phase shift matrices,” *IEEE Trans. Veh. Technol.*, vol. 71, no. 6, pp. 6367–6383, Jun. 2022.
- [17] G. M. Rebeiz and J. B. Muldavin, “RF MEMS switches and switch circuits,” *IEEE Microw. Mag.*, vol. 2, no. 4, pp. 59–71, 2001.
- [18] L. Zhang, X. Q. Chen, R. W. Shao *et al.*, “Breaking reciprocity with space-time-coding digital metasurfaces,” *Advanced Materials*, vol. 31, no. 41, p. 1904069, 2019.
- [19] L. Zhang, X. Q. Chen, S. Liu *et al.*, “Space-time-coding digital metasurfaces,” *Nature communications*, vol. 9, no. 1, p. 4334, 2018.
- [20] A. Li, S. Singh, and D. Sievenpiper, “Metasurfaces and their applications,” *Nanophotonics*, vol. 7, no. 6, pp. 989–1011, 2018.
- [21] C. Liaskos, G. G. Pyrialakos, A. Pitilakis *et al.*, “The internet of metamaterial things and their software enablers,” *Int. Telecommun. Union J.*, vol. 1, no. 1, pp. 55–77, 2020.
- [22] F. Rusek, J. Flordelis, E. Bengtsson *et al.*, “Spatially selective reconfigurable intelligent surfaces through element permutation,” in *Proc. IEEE Int. Conf. Commun. (ICC)*, Denver, USA, 2024, pp. 5540–5545.
- [23] G. Pan, J. Ye, J. An *et al.*, “Full-duplex enabled intelligent reflecting surface systems: Opportunities and challenges,” *IEEE Wireless Commun.*, vol. 28, no. 3, pp. 122–129, Jun. 2021.
- [24] H. Wang, Z. Han, and A. L. Swindlehurst, “Channel reciprocity attacks using intelligent surfaces with non-diagonal phase shifts,” *IEEE Open J. of the Comm. Society.*, 2024.
- [25] Z. Liu, H. Li, and B. Clerckx, “Non-reciprocal BD-RIS in full-duplex communications: A perspective on sum-rate maximization,” *arXiv preprint arXiv:2411.18523*, 2024.
- [26] Z. Liu and B. Clerckx, “A secure full-duplex wireless circulator enabled by non-reciprocal beyond-diagonal RIS,” *arXiv preprint arXiv:2507.23381*, 2025.
- [27] W. Tang, M. Z. Chen, X. Chen *et al.*, “Wireless communications with reconfigurable intelligent surface: Path loss modeling and experimental measurement,” *IEEE Trans. Wireless Commun.*, vol. 20, no. 1, pp. 421–439, Jan. 2021.
- [28] A. Sayeed, “Deconstructing multiantenna fading channels,” *IEEE Trans. Sig. Proc.*, vol. 50, no. 10, pp. 2563–2579, Oct. 2002.
- [29] J. Tian, Y. Han, S. Jin *et al.*, “Near-field channel reconstruction in sensing RIS-assisted wireless communication systems,” *IEEE Trans. Wireless Commun.*, vol. 23, no. 9, pp. 12 223–12 238, Sep. 2024.
- [30] C. Liaskos, S. Nie, A. Tsioliardou *et al.*, “A new wireless communication paradigm through software-controlled metasurfaces,” *IEEE Commun. Mag.*, vol. 56, no. 9, pp. 162–169, 2018.
- [31] H. Zhang, N. Shlezinger, F. Guidi *et al.*, “Beam focusing for near-field multiuser MIMO communications,” *IEEE Trans. Wireless Commun.*, vol. 21, no. 9, pp. 7476–7490, 2022.
- [32] W. L. Stutzman and G. A. Thiele, *Antenna theory and design*. John Wiley & Sons, 2012.
- [33] Int. Telecommun. Union, “Propagation data and prediction methods required for the design of Earth-space telecommunication systems,” International Telecommunication Union, Geneva, Switzerland, ITU-Recommendation P.618-13, Dec. 2017.
- [34] ———, “Specific attenuation model for rain for use in prediction methods,” International Telecommunication Union, Geneva, Switzerland, ITU-Recommendation P.838-3, Mar. 2005.
- [35] Z. Liu, A. Bhandari, and B. Clerckx, “Full-duplex beyond self-interference: The unlimited sensing way,” *IEEE Commun. Lett.*, 2024.
- [36] K. Shen and W. Yu, “Fractional programming for communication systems—Part I: Power control and beamforming,” *IEEE Trans. Sig. Proc.*, vol. 66, no. 10, pp. 2616–2630, 2018.
- [37] J. H. Manton, “Optimization algorithms exploiting unitary constraints,” *IEEE Trans. Sig. Proc.*, vol. 50, no. 3, pp. 635–650, 2002.
- [38] Q. Shi and M. Hong, “Penalty dual decomposition method for non-smooth nonconvex optimization—Part I: Algorithms and convergence analysis,” *IEEE Trans. Sig. Proc.*, vol. 68, pp. 4108–4122, 2020.
- [39] E. Everett, C. Shepard, L. Zhong *et al.*, “SoftNull: Many-antenna full-duplex wireless via digital beamforming,” *IEEE Trans. Wireless Commun.*, vol. 15, no. 12, pp. 8077–8092, 2016.